Pore system characterization of organic-rich shales using nanoscale-resolution 3D imaging

Jan Goral [a], Ian Walton [a], Matthew Andrew [b], Milind Deo [a]

[a] *Department of Chemical Engineering, University of Utah, Salt Lake City, Utah, USA*

[b] *Carl Zeiss X-Ray Microscopy, Pleasanton, California, USA*

Abstract

The Vaca Muerta Shale in Argentina is the first major commercial shale oil/gas play outside of North America. High-resolution 2D/3D imaging of shale rocks for the purpose of establishing their mineralogy, total, and connected porosities has become more and more sophisticated. In this paper, nanoscale-resolution focused ion beam (FIB)–scanning electron microscopy (SEM) nano-tomography was used to obtain images of pore structures within two organic-rich regions of interest (ROIs), selected based on correlative SEM and automated mineralogy maps. Advanced machine learning classification tools were used to segment the images and assign porosities and other components. Pore size distribution and pore connectivity analyzes revealed that about 95% of all the pores, present within the two ROIs, had a diameter of less than approximately 75 nm, and that most of these pores were poorly connected. In a similar fashion, the flow rate distribution analysis showed that pores with diameters of about 150 to 330 nm contributed to over 50% of the flow capacity of the connected pore systems. These results suggest that although most of the pores typically found in shales have pore diameter smaller than about 100 nm, most of the hydrocarbon production is carried by a relatively small number of larger connected pores with pore diameter greater than about 150 nm. This study implies that a large portion of the organic-hosted pores (with diameter typically smaller than about 100 nm) do not provide permeable flow pathways for the oil and/or gas migration, and hence have very little contribution to the hydrocarbon production.

Keywords: Porosity and Permeability of Shales; Multi-Scale Imaging; Correlative Microscopy; Machine Learning Image Segmentation; Digital Rock; Vaca Muerta Shale

1. Introduction

Over the past couple of decades, oil and/or gas production from unconventional (shale) reservoirs has become very important to the U.S. and Canadian economies, and is likely to assume great importance to other countries worldwide with substantial shale oil and gas resources, such as Argentina (Vaca Muerta Shale) (Badessich et al., 2016). Among the key factors in assessing the oil/gas productivity potential of shale reservoirs (also referred to as shales) are their porosity and permeability. Specifically, we need to understand where the hydrocarbons are stored and to identify their predominant flow pathways. Typically, shale porosity is less than 5%, and shale permeability is less than 1,000 nD. The nature of the rock fabric in determining the effective values of these petrophysical properties is attracting a great deal of attention from the research community.

Different fluids (such as oil, gas, or water) occur in the pore spaces inside or between individual organic and non-organic (mineral) grains, and/or are adsorbed into their matrix (Ji et al., 2012; Zhang et al., 2012). These pores, with diameters that typically range between a few nanometers (typical for organic pores) to a couple of micrometers (typical for mineral pores), create connected (effective) and non-connected (isolated) pore systems. Effective pore systems connect to the natural and/or induced fracture networks that ultimately connect to the wellbore. In shales, understanding intricate pore/fracture networks, their geometry, connectivity, and distribution (both within organic and mineral matrix) are key factors affecting hydrocarbon storage and production mechanisms (Slatt et al., 2011). These complex flow pathways have been of interest to many petroleum industry and academia research and development groups, which study continuum and non-continuum fluid flow and transport phenomena in shales (e.g., Mehmani et al., 2013; Shabro et al., 2011; Xia et al., 2017, 2019; Zhang et al., 2015). Although there is significant interest in fluid flow and transport phenomena modeling and simulation in organic/mineral pore network 2D/3D models, there is limited study focused on investigating the actual realistic ("real-world") shale pore systems responsible for oil and/or gas production. Because fluid flow and transport phenomena in shales depend on their nanoporous microstructure and the interconnectivity of their pores, characterizing effective (and isolated) pore systems along with the organic and mineral matter surrounding these pores is critical for understanding hydrocarbon storage and/or production mechanisms.

In this paper, using digital rock 3D models reconstructed from machine-learning segmented focused ion beam scanning electron microscopy (FIB-SEM) nano-tomography image datasets (collected at ultra-high-resolution – voxel size: 2.5 nm x 2.5 nm x 5 nm), the impact of typical pore size distribution on estimates of the effective porosity and flow rate in shales was investigated. This study, and the results published elsewhere (Walton, 2019), show that although most of the pores typically found in shales have pore diameter smaller than about 100 nm, most of the hydrocarbon production is carried by a relatively small number of larger connected pores with pore diameter greater than about 150 nm. Thus, the petroleum industry tends to overestimate the effective porosity (defined in terms of the pore volume that may be produced in a "reasonable" time frame as opposed to the total porosity). Furthermore, it is suggested that currently becoming more popular, fluid flow modeling and simulation studies that focus on nanometer-sized pores (often found in organic matter) may be misplaced – these pores may be abundant, but are relatively unimportant as far as productivity is concerned.

1.1.Background

Shales (fine-grained sedimentary rocks) are intrinsically complex and heterogeneous, consisting of interlaminated organic matter, mineral matter, and pores within or between these nanometer- to micrometer-sized grains. Depending on the depositional environment, there are two types of organic matter that can be found in shales: land-derived and aquatic-derived. Organic matter (kerogen and/or bitumen) is compressed and heated deep within Earth over geologic time, to form hydrocarbons including oil, condensate, and wet/dry natural gas. The amount of oil and/or gas generated is determined by the kerogen type and the heating rate (thermal maturity) (Pommer and Milliken, 2015; Song et al., 2019). Commonly occurring mineral matter (minerals) in shales can be categorized into five main categories: silicates, carbonates, phosphates, sulfides, and sulfates. The most common silicates include phyllosilicates (with clay, mica, and chlorite groups) and tectosilicates (with quartz and feldspar groups). Carbonates, on the other hand, can be sub-divided into calcite and dolomite groups (Klein et al., 2007). More detailed classification of commonly found minerals in shales is presented in Fig. 1.

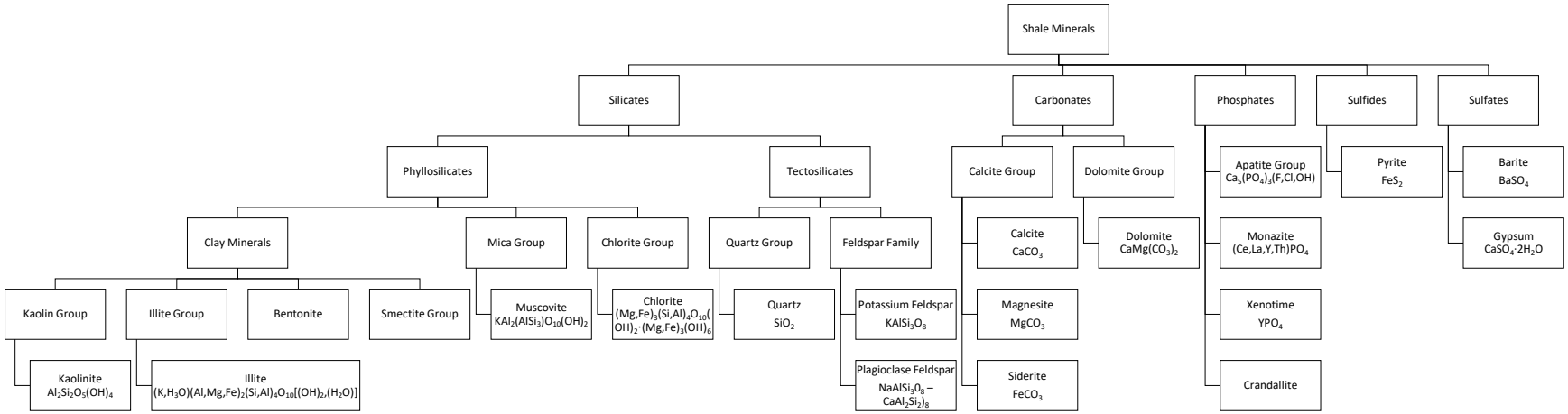

Fig. 1. Commonly found minerals in shales and their classification.

Both the organic and mineral matter, in shales, have a variety of pore systems that can be any combination of pore types of different pore sizes – from a few nanometers to several micrometers in size. Typical shales are characterized by their small pores, and hence their very low porosity (pore volume) and permeability. A considerable amount of effort has gone into measuring and characterizing the pore volume both within the organic and mineral shale rock matrix (Anovitz and Cole, 2015; Goral et al., 2016; Milliken et al., 2013; Milliken and Curtis, 2016).

According to the International Union of Pure and Applied Chemistry (IUPAC), there are three types of pores classified based on their size: Micropores are defined as pores less than 2 nm in diameter, mesopores have diameter in the 2-50 nm range, and macropores have diameter in excess of 50 nm. Loucks et al. (2012) have proposed an alternative classification which is compared with the IUPAC system in Fig. 2. In shales, most pores appear to fall into Loucks' nanopore category. In their analysis of pore types in the Barnett Shale, Loucks et al. (2009) grouped the pores into two categories: micropores (having diameter > 0.75 μm) and nanopores (having diameter < 0.75 μm). They noted that the nanopores are by far the most abundant pore type in the Barnett Shale, and that most of them are located within the organic matter. On the basis of capillary-pressure analysis, they concluded that the size of most pores is actually much smaller – in the 5-15 nm range – and fall into the nanopore category. Typical pore throat sizes in siliciclastic rocks are shown in Fig. 3 (taken from Nelson (2009)). Note that pore throats of shales, in his study, vary in size from about 5 nm to 100 nm in diameter. For comparison, note that the molecular diameters of water, mercury, and free gases are at least an order of magnitude smaller than even the smallest pore throats.

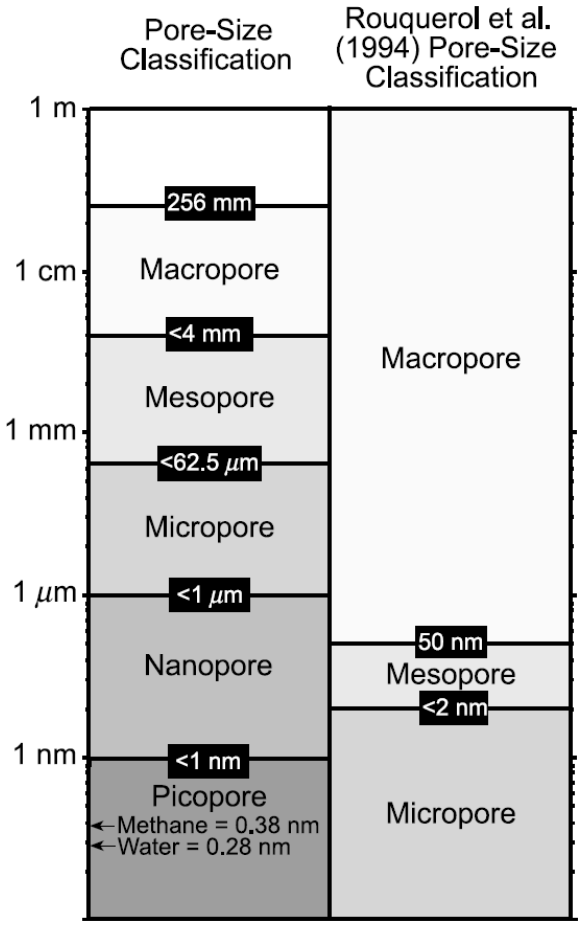

Fig. 2. Pore classification (from Loucks et al. (2012)).

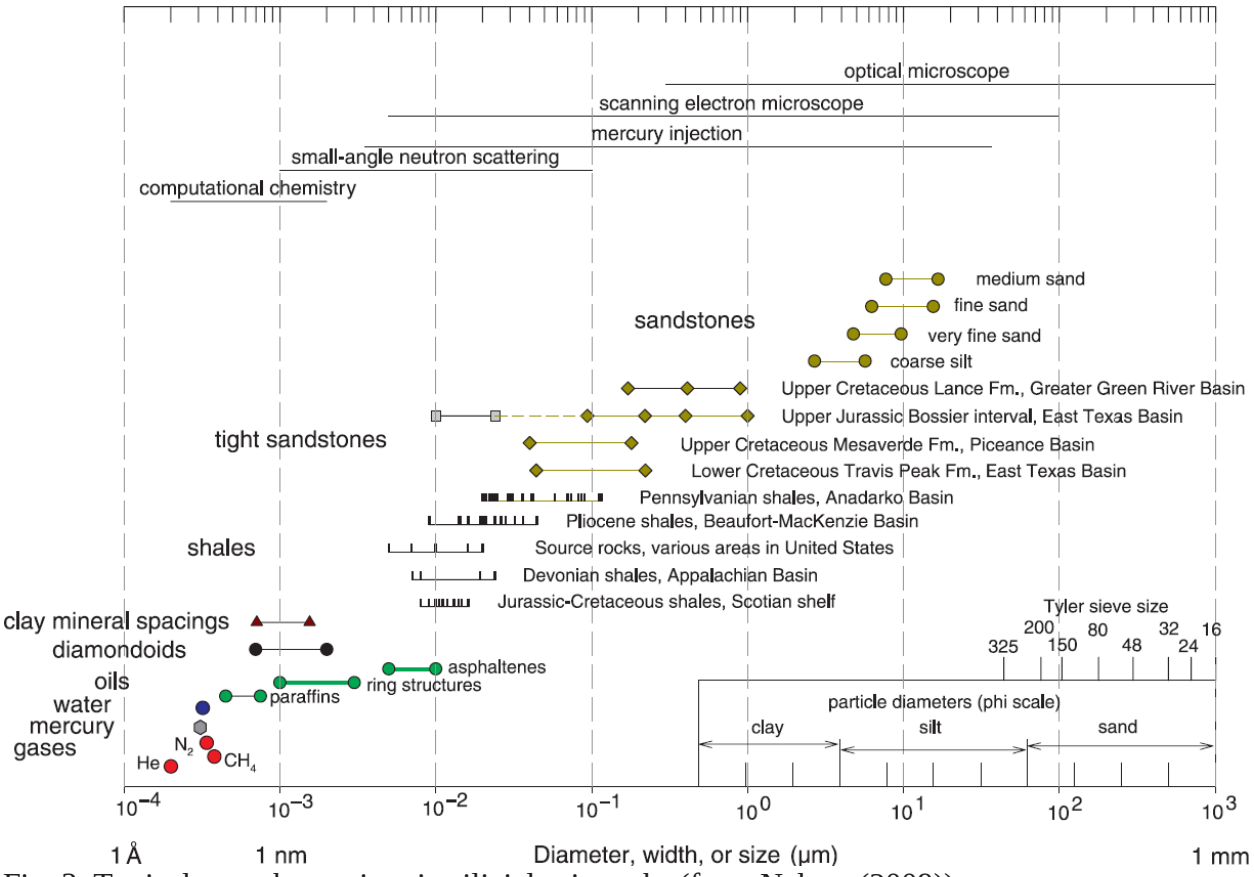

Fig. 3. Typical pore throat sizes in siliciclastic rocks (from Nelson (2009)).

Additionally, there are three main categories of pore types in shale rock matrix classified based on their relationship with grains: organic-matter intragranular (intraparticle) pores (also referred to as organic-hosted pores), mineral-matter intraparticle pores (also referred to as mineral-hosted pores), and mineral-matter intergranular (interparticle) pores. Interparticle pores are located between grains, whereas intragranular pores are found within particles. Goral at al. (2015a) visualize these four types of pores in 3D (as shown in Fig. 4) and quantify organic-hosted pores in the Marcellus Shale. Goral et al. (2015b), on the other hand, quantify interparticle pores at the (weak) interphase of organic and mineral matter, and indicate that these pores predominantly contribute to the effective porosity of the Woodford Shale. Organic-matter intragranular pores appear to be related to thermal maturation of organic matter, whereas mineral-matter intraparticle and interparticle pores are strongly affected by mechanical and chemical diagenesis (Curtis et al., 2011a, 2012a). Organic-rich shales with high total organic carbon (TOC) and thermal maturity often have high organic porosity because the conversion from kerogen or bitumen to hydrocarbons often leads to an increase in porosity.

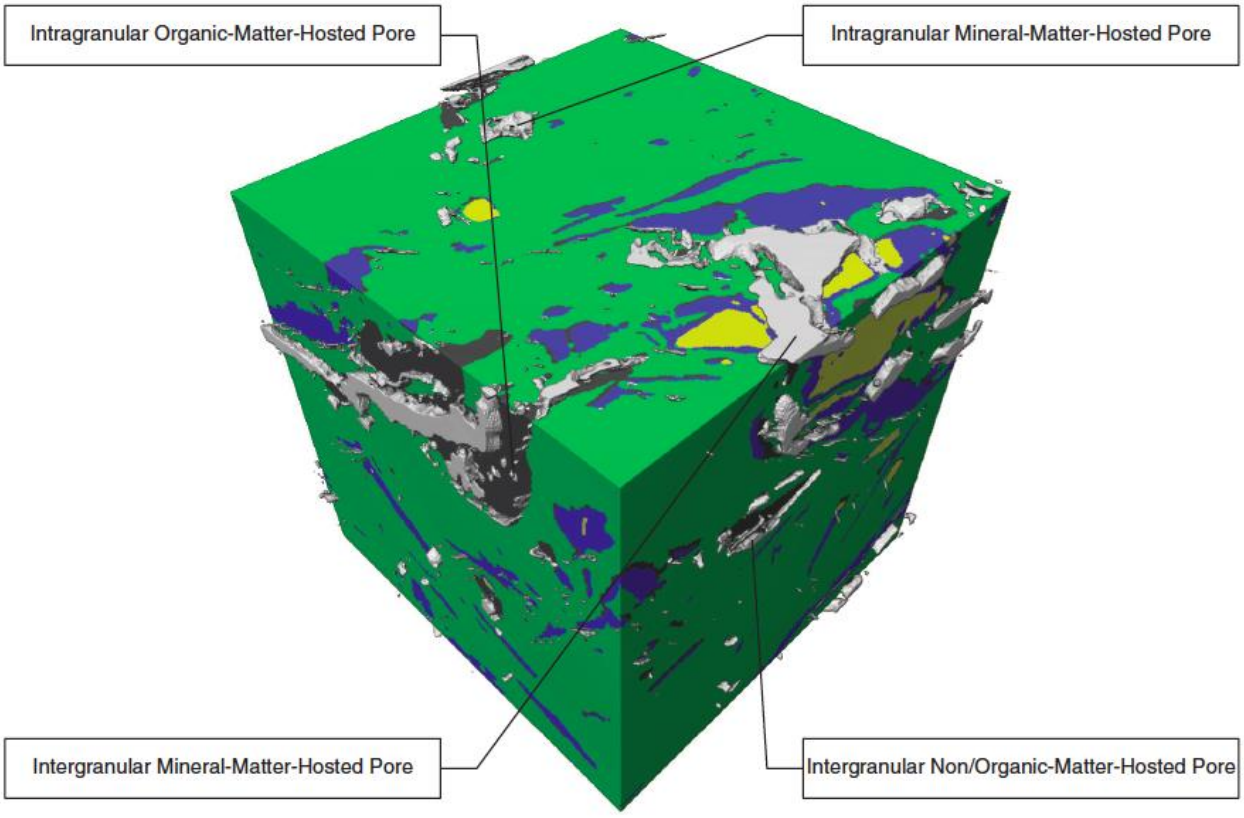

Fig. 4. Commonly found pores in shales and their classification (from Goral et al. (2015a)).

It is commonly believed by the petroleum industry that organic-hosted pores are responsible for the hydrocarbon production. It is often stated that the variation of kerogen/bitumen or TOC within different shales is important in distinguishing their oil/gas productivity potential. Others have suggested that since gas transport from the organic-hosted pores to the connected pore/fracture networks depends on the very slow processes of diffusion and desorption, gas production from this source can be neglected on any reasonable time scale.

In this study, and the results published elsewhere (Goral el al., 2015ab, 2016, 2018), there is significant evidence to support that organic-hosted pores tend to act as separate 'nano-reservoirs' isolated from each other. These pores, surrounded by the organic matter (which also tend to be isolated from each other), are characterized by their very small size (< 20 nm) and limited connectivity, as shown in the example transmission electron microscopy (TEM) image of the pure organic matter (lifted-out using FIB-SEM) below in Fig. 5.

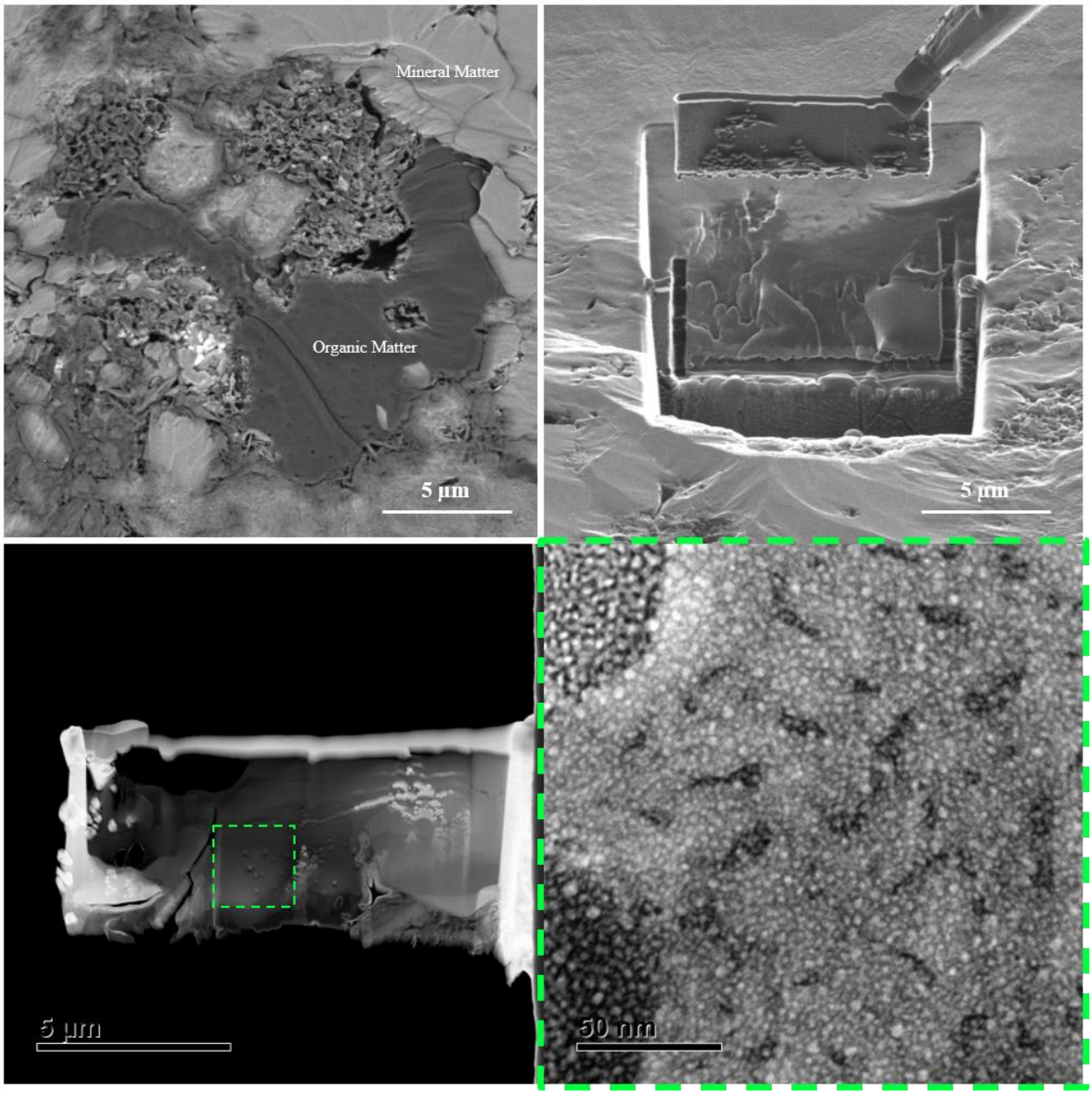

Fig. 5. Scanning / transmission electron microscopy (S/TEM) image of organic-hosted pores within pure organic matter (TEM lamella) lifted-out using FIB-SEM.

2. Methods and Experimental Procedure

Traditional laboratory methods for the measurement of porosity (such as mercury intrusion porosimetry (MIP)) and permeability of reservoir-rocks (such as pressure pulse decay) have been applied to ultra-tight shale source-rocks with limited success. Many of the problems are associated with the high resistance to fluid flow (mercury injection, or simply gas or liquid flow) through the narrow pores and with sample-preparation artifacts (such as narrow stress-relief cracks) that dominate the measurements. Recently, modern 2D/3D imaging techniques, such as nanoscale-resolution field-emission SEM (FE-SEM), FIB-SEM, S/TEM, or helium ion microscopy (HIM), have been used to investigate pore systems in shales in very fine detail, down to the sub-nanometer level (Cavanaugh and Walls, 2016; Chalmers et al., 2012; Curtis et al., 2011b, 2012b; Driskill et al., 2013; Goral et al. 2018, 2019; Loucks and Reed, 2014). These methods have facilitated characterization of the pore morphology (in 3D) of both the organic matter (i.e. kerogen and bitumen) and non-organic (mineralogical) components of shales.

2.1.Correlative Multi-Scale Imaging

In this study, the entire top surface of a 2.5-cm diameter core-plug end-trim of the Vaca Muerta Shale rock sample was first initially imaged with a ZEISS Auriga FIB-SEM with 402 nm/pixel resolution. Next, based on this SEM mosaic image (map), a smaller approximately 1.2 mm x 1.2 mm region of interest (ROI) was imaged with the same system with 40 nm/pixel resolution. Both the low- and high-resolution SEM tile-sets were acquired (and stitched) using the Atlas 5 software. SEM map imaging allows to image a much larger field of view (FOV) at much higher resolution. Additionally to the above two SEM maps, an overlapping 1.57 mm x 1.57 mm ROI was imaged with a ZEISS Mineralogic Reservoir automated mineralogy system – Zeiss Sigma VP SEM with two Bruker energy-dispersive X-ray spectroscopy (EDS) detectors – with 1 μm/pixel resolution. Automated mineralogy identifies and quantifies minerals present within a rock based of their elemental analysis with EDS. The EDS data in combination with SEM back-scattered electron (BSE) image is then converted into a mineral map. The above SEM maps and automated mineralogy map were manually correlated (superimposed) with each other using the Zen Connect software, as shown in Fig. 6.

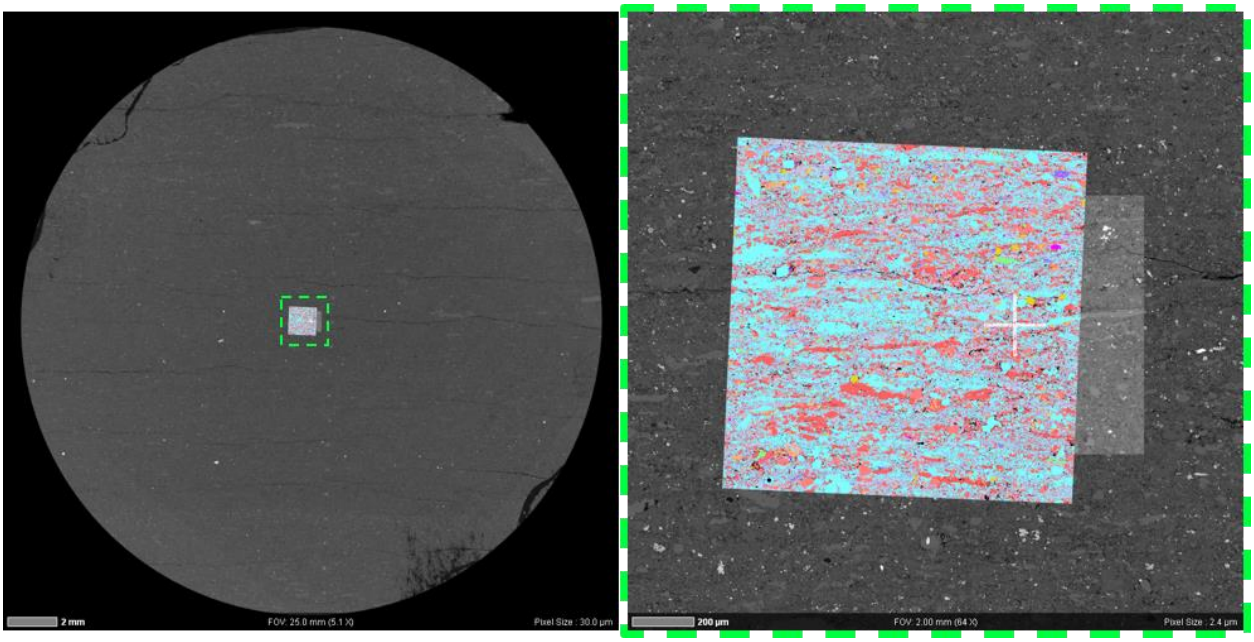

Fig. 6. Visualization of the correlated low-resolution (402 nm/pixel) SEM map of the entire top surface of 2.5-cm diameter core-plug end-trim, high-resolution (40 nm/pixel) SEM map of 1.2 mm x 1.2 mm ROI, and 1-µm/pixel resolution automated mineralogy map of 1.57 mm x 1.57 mm ROI – see Fig. 7 for complete color legend.

Based on the above maps, two organic-rich ROIs were selected and imaged in 3D with a ZEISS Crossbeam 550 FIB-SEM with an anisotropic voxel size of 2.5 nm x 2.5 nm x 5 nm. Table 1 summarizes dimensions of the two ROIs along with the resolution at which these volumes were imaged. Note that neither of these two ROIs can be considered representative of the entire rock sample's porosity nor mineralogy – they were selected and imaged in order to characterize nanometer-sized pores (in 3D) present within the organic matter. FIB-SEM nano-tomography is the only nanoscale-resolution 3D imaging technique that allows for such characterization.

Table 1. Dimensions of the ROI-1 and ROI-2 along with the resolution at which these two volumes were imaged with FIB-SEM.

	Resolution	Dimensions (X)	Dimensions (Y)	Dimensions (Z)
FIB-SEM ROI-1	2.5 x 2.5 x 5 nm	5.125 μm	4.25 μm	3 μm
FIB-SEM ROI-2	2.5 x 2.5 x 5 nm	5.375 μm	3.75 μm	3.5 μm

3. Results and Discussion

3.1.Quantitative SEM and Automated Mineralogy Image Analysis

The SEM and automated mineralogy maps revealed high heterogeneity of the investigated Vaca Muerta Shale rock sample composed of various minerals, organic matter, and pores within and/or between these components. The automated mineralogy map (Fig. 7) showed 46% silicate, 34% carbonate, and 20% clay minerals, as shown in ternary diagram in Fig. 8. Table 2 presents, in detail, the automated mineralogy results. Note that EDS-based automated mineralogy is limited to approximately 1 μm/pixel spatial resolution which is defined by the size of the interaction volume – the region of X-ray excitation in the sample determined by the density of the sample, and the accelerating voltage used during the EDS microanalysis (Goldstain et al. 2017). Therefore, organic/mineral grains and/or pores smaller than 1 micron could not be resolved. Only larger micro-pores/-fractures, organic and mineral grains were quantified. A high-resolution (40 nm/pixel) SEM map, on the other hand, was able to captured smaller features (e.g., nanometer-sized organic pores). Note that although the high-resolution SEM map showed high organic porosity within the investigated rock sample, SEM 2D imaging fails to provide 3D pore structure information necessary for pore connectivity analysis. Therefore, in order to fully characterize shale pore systems (and understand their impact on hydrocarbon storage and/or production mechanisms), high-resolution 3D imaging (with e.g., FIB-SEM nano-tomography) is essential.

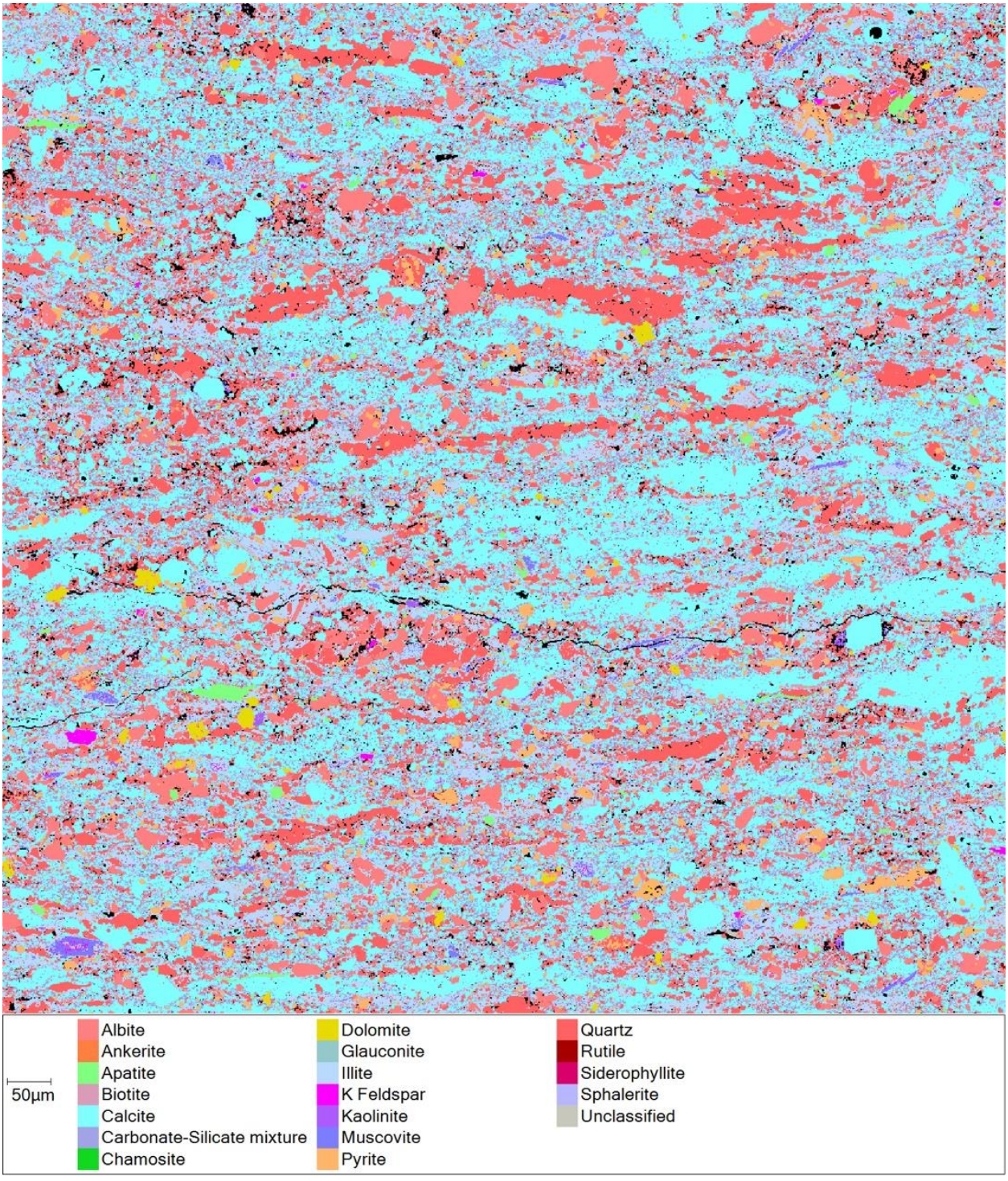

Fig. 7. Automated mineralogy map of 1.57 mm x 1.57 mm ROI.

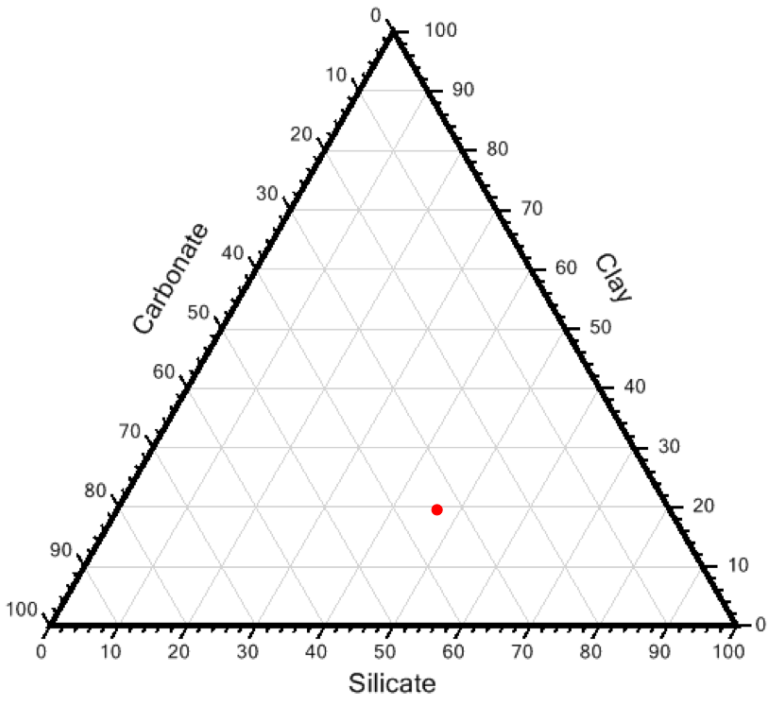

Fig. 8. Ternary diagram generated based on the automated mineralogy map.

Table 2. Minerals (together with their surface area and average grain size) present within the automated mineralogy map. Note, sum of totals may not equal 100% because of independent rounding.

Mineral	**Surface Area [%]**	**Average Grain Size [µm]**
Calcite	35.3	5.4
Quartz	19.1	3.5
Illite	15.2	3.5
Carbonate-Silicate Mixture	13.5	2.6
Albite	7.1	4.1
Pyrite	2.8	3.7
Micrometer-Sized Pores and/or Fractures	3.06	5.5
Other	3.9	-

3.2.Quantitative FIB-SEM Image Analysis

3.2.1. Image Processing and (Machine Learning) Image Segmentation

One of the biggest challenges in quantitative image analysis is that of segmentation – discretization of an image into its constituent phases. This is because raw greyscale datasets usually contain a series of modality-specific artefacts, as well as random noise. As these artefacts become more complex (or noise levels increase), traditional segmentation techniques, such as global greyscale thresholding (e.g., Otsu, 1979) or local region growing (e.g., Jones et al., 2007) begin to fail. An even greater challenge is that of "textural contrast" – that when a scientist inspects an image, they extract features beyond simple greyscale contrast, but include features such as structural size, shape, and internal consistency. Over the last twenty years, machine learning has found application in a wide array of fields ranging from stock market analysis to medical diagnosis; however, its application to microscopy and microanalysis generally has only developed recently (Chauhan et al., 2016; Koebernick et al., 2017; Schweizer et al., 2018). Recent benchmarking studies (Andrew, 2018; Berg et al., 2018) have shown that machine-learning classification tools strongly outperform traditional segmentation techniques as noise levels increase, particularly for complex multiphase images. This is because it allows for datasets to be classified based on multiple independent features (e.g., local and non-local greyscale, greyscale gradient, and textural features) in a complex multi-variant classifier, rather than performing relatively simple classifications based on a small number of features.

In this study, first, image processing was used to improve image quality of the FIB-SEM nano-tomography image datasets. In this process, a combination of different standard operations (e.g., image sequence registration/alignment and cropping) and filters (e.g., NLM and FFT filters) was applied to remove noise, blur, and other background intensity variations from the FIB-SEM nano-tomography image datasets. Second, the image datasets were segmented, using machine learning, into segments representing different phases – groups of features of the rock microstructure (e.g., pores or minerals). Preliminary image processing was performed using the Dragonfly Pro software, whereas image segmentation was performed using the ZEN software with the Intellesis machine learning image segmentation platform – a graphical interface allowing for interactive training of machine learning classifiers from microscopy image datasets. It uses open-source packages for both feature extraction (scikit-image (www.scikit-image.org) and SciPy (www.scipy.org)), multivariant classifier construction, simplification and application (scikit-learn

(www.scikit-learn.org)), and task scheduling (Dask (www.dask.pydata.org/en/latest/)). The interface allows for a direct and interactive "painting" of training data onto an image. Thirty-three features are then extracted from each greyscale channel, including 20 Gaussian filters (with standard deviations ranging from 0.7 to 8 pixels), five mean filters (of similarly varying kernel size), four Gabor filters (with two values for standard deviation (1 and 3) and two wavelengths (5 and 10 pixels)), one Hessian filter (giving three feature vectors corresponding to the xx, xy, and yy second-order partial derivatives), and one Sobel feature vector. A multivariant classifier is then trained on these features using a "forest of randomized trees" approach (Breiman, 2001). This classifier is then applied to either the current 2D slice displayed for a 3D volume or a local region in a large 2D image. The user then iteratively adds or removes training data on multiple 2D slices through the 3D volume until a visually satisfactory segmentation is found. Once a desirable model has been trained, it can be applied across the entire 3D volume, producing the final image segmentation.

Phases such as pores, organic matter, and mineral matter (including silicate, carbonate, and sulfide minerals) were segmented and quantified. An example of machine-learning image segmentation of one of the images ("slices") of the FIB-SEM ROI-1 and ROI-2 nano-tomography image datasets is presented in Fig. 9 and Fig. 10, respectively.

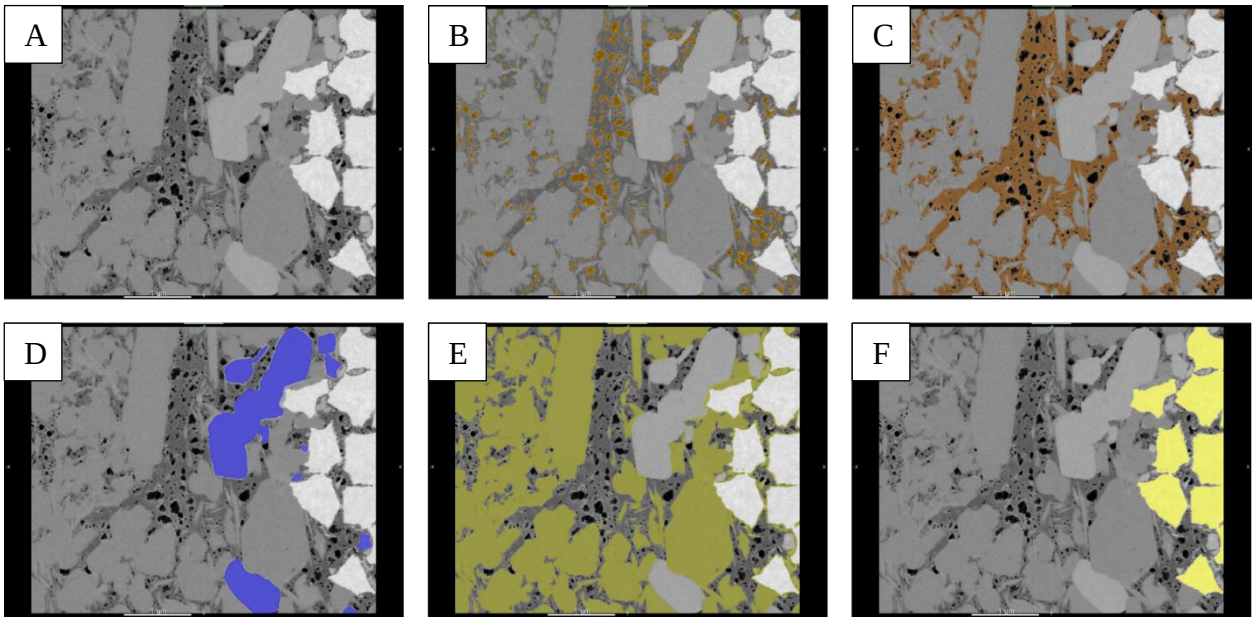

Fig. 9. An example of machine-learning image segmentation of one of the images ("slices") of the FIB-SEM nano-tomography image dataset of the ROI-1. Starting from top left, image (A) depicts non-segmented image ("slice"), image (B) depicts segmented pores, image (C) depicts

segmented organic matter, image (D) depicts segmented carbonate, image (E) depicts segmented silicate, and image (F) depicts segmented sulfide.

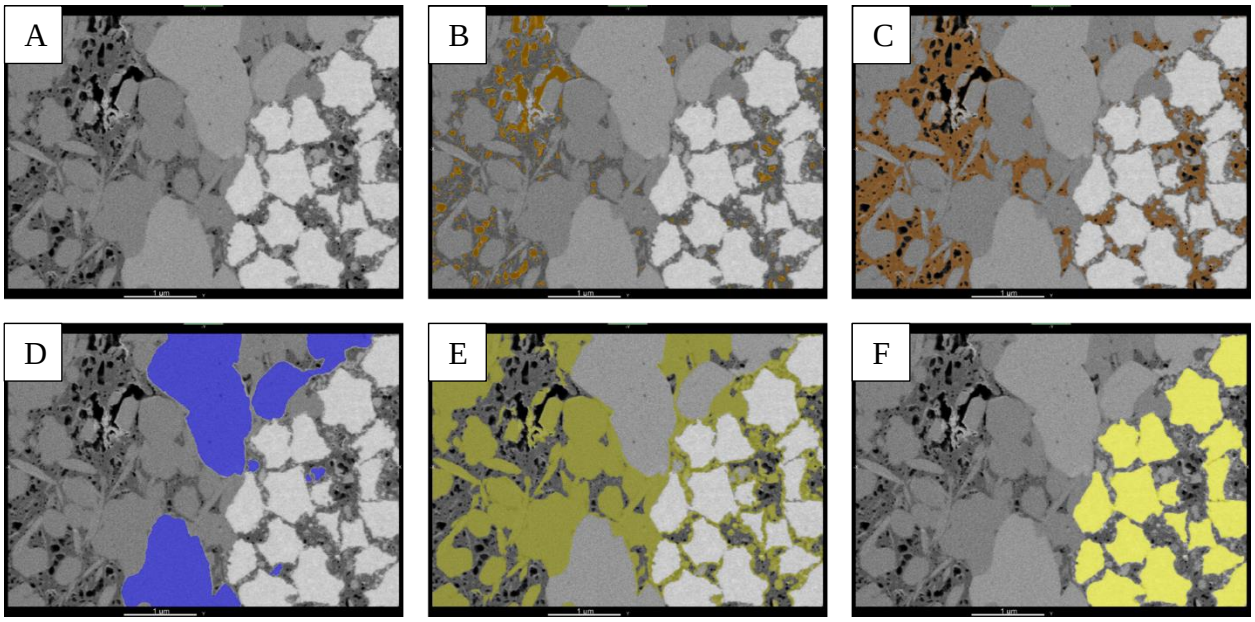

Fig. 10. An example of machine-learning image segmentation of one of the images ("slices") of the FIB-SEM nano-tomography image dataset of the ROI-2. Starting from top left, image (A) depicts non-segmented image ("slice"), image (B) depicts segmented pores, image (C) depicts segmented organic matter, image (D) depicts segmented carbonate, image (E) depicts segmented silicate, and image (F) depicts segmented sulfide.

Fig. 11 and Fig. 12 depict visualization of digital rock 3D models reconstructed from segmented FIB-SEM image datasets. The volume fractions of the pore, organic and mineral phases are summarized in Table 3.

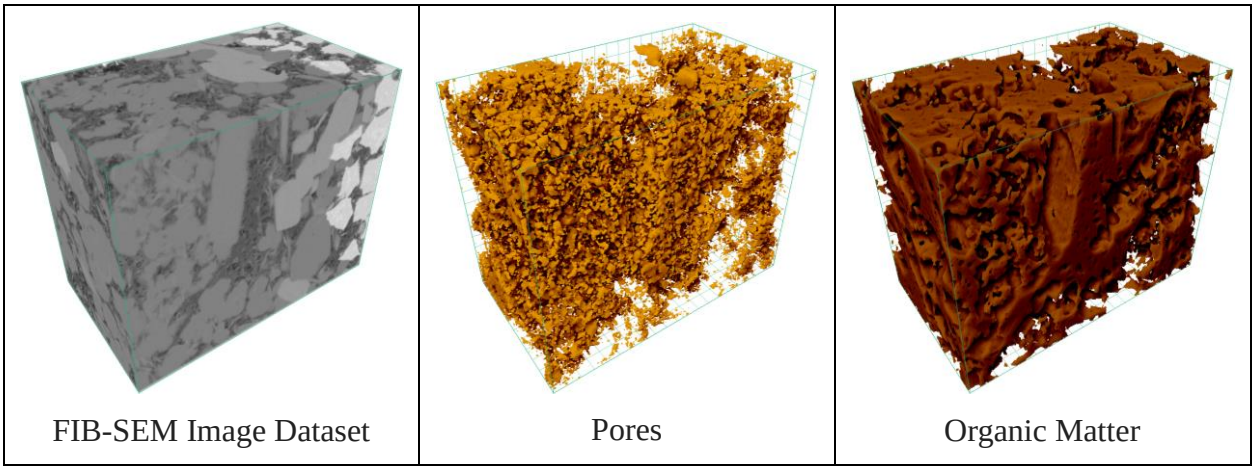

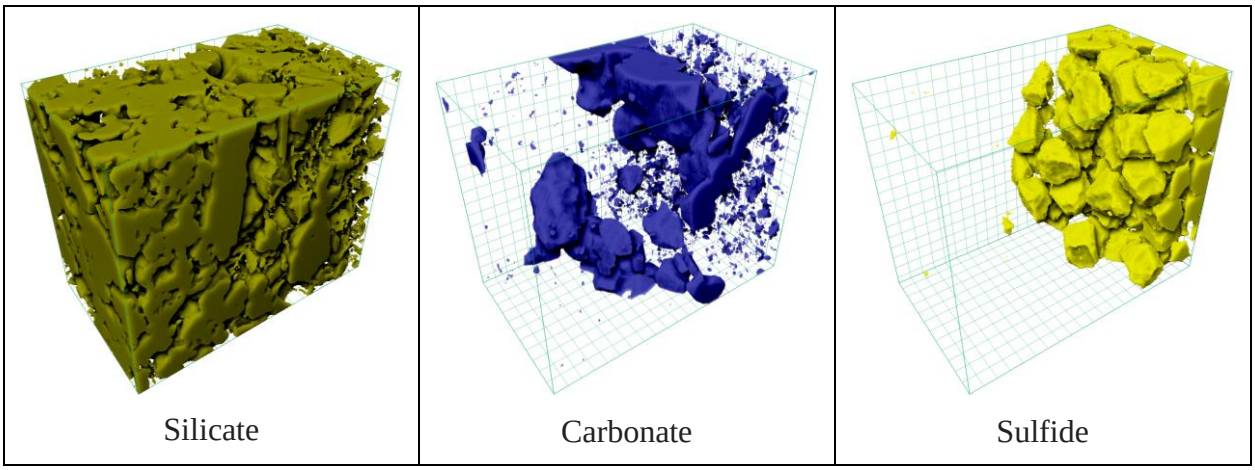

Fig. 11. Visualization of segmented pores, organic matter, silicates, carbonates, and sulfides reconstructed from FIB-SEM nano-tomography image dataset of the ROI-1.

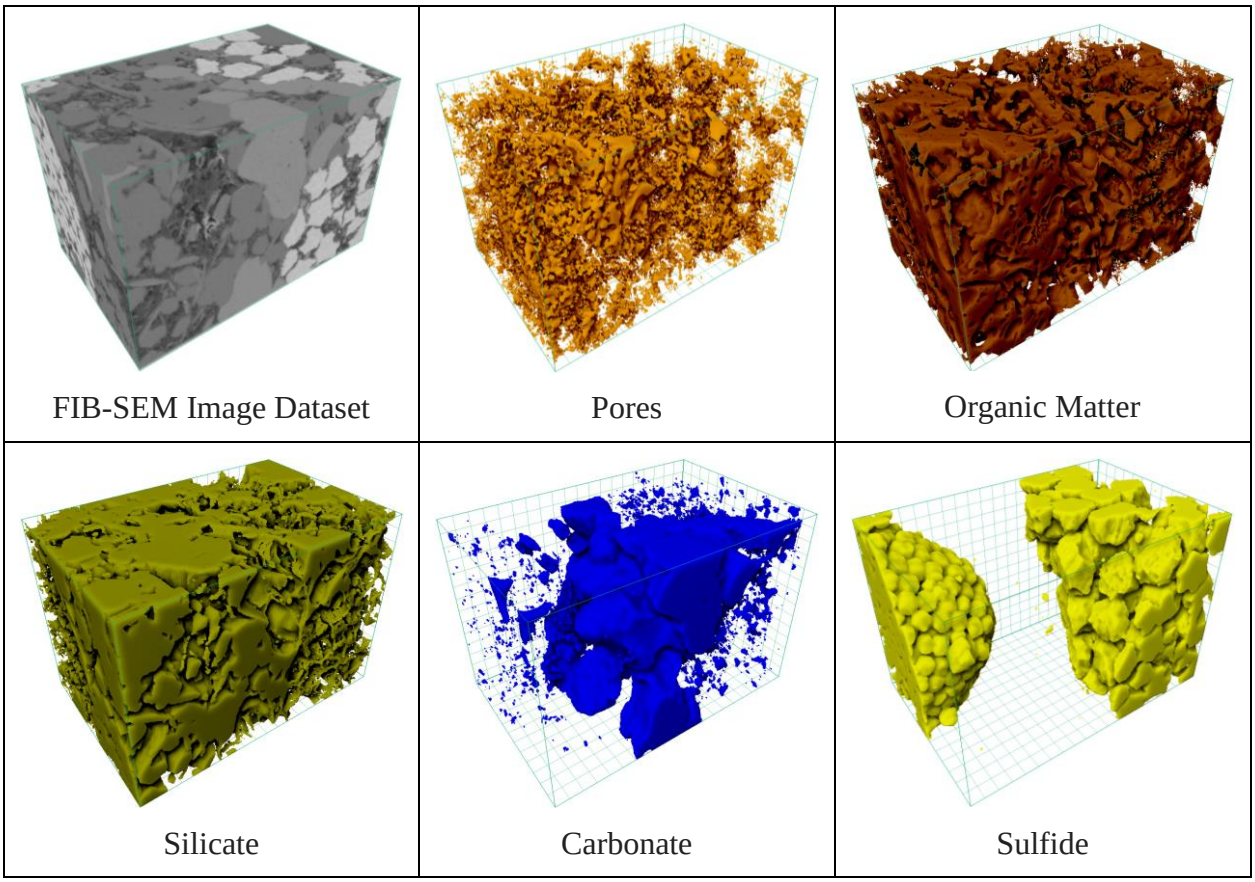

Fig. 12. Visualization of segmented pores, organic matter, silicates, carbonates, and sulfides reconstructed from FIB-SEM nano-tomography image dataset of the ROI-2.

Table 3. Volume fractions of the pore, organic, carbonate, silicate, sulfide phases present within the digital rock 3D models reconstructed from FIB-SEM nano-tomography image datasets of the ROI-1 and ROI-2. Note, sum of totals may not equal 100% because of independent rounding.

	Pore Phase	**Organic Phase**	**Carbonate Phase**	**Silicate Phase**	**Sulfide Phase**
FIB-SEM ROI-1	6.9	24%	7.5%	45.6%	16.1%
FIB-SEM ROI-2	3.7	14.4	12.7	41.2	27.9

As shown in Table 3, volume fractions of pore, organic, or mineral phases within the FIB-SEM ROI-1 were different from those of FIB-SEM ROI-2. This is because of relatively small volumes that were imaged with FIB-SEM, which cannot be considered representative of the shale rock sample, due to its high heterogeneity. Although it is extremely difficult to get quantitative information about porosity or mineralogy of these rocks, their qualitative information (such as pore or grain size distribution) should remain the same.

In the next section, using the above segmented (pore) digital rock 3D models, connected (effective) and non-connected (isolated) porosities are separated out, quantified, and compared with each other in terms of their pore size distribution.

3.2.2. *Pore Connectivity and Pore Size Distribution Analysis*

As seen in Fig. 13 and Fig. 14, the total porosity of the two 3D models was separated out into connected (effective) and non-connected (isolated) pores. The effective porosity – 4.2% (FIB-SEM ROI-1) and 1.7% (FIB-SEM ROI-2) – was determined based on its connectivity to boundaries of the 3D model; Any pore that was connected to the 3D model boundary box was considered as a connected pore (since there was a chance that it could be connected to a larger pore system outside of this box, which was not captured with FIB-SEM). The remaining pores were considered isolated pores. In reservoir characterization, total porosity is used for overall hydrocarbon storage assessment, while effective porosity is used for hydrocarbon production assessment. It is therefore important to gain insights into both types of porosity.

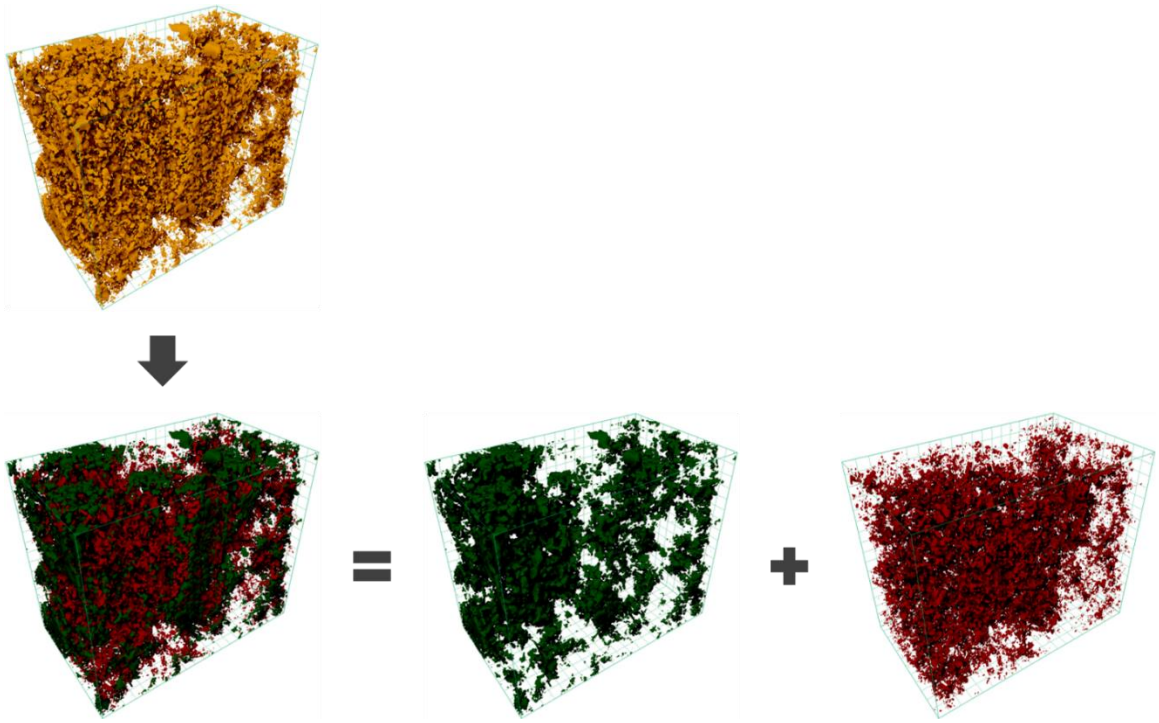

Fig. 13. Total porosity (yellow-colored 3D model) of the ROI-1 separated into connected (effective) porosity (green-colored 3D model) and non-connected (isolated) porosity (red-colored 3D model).

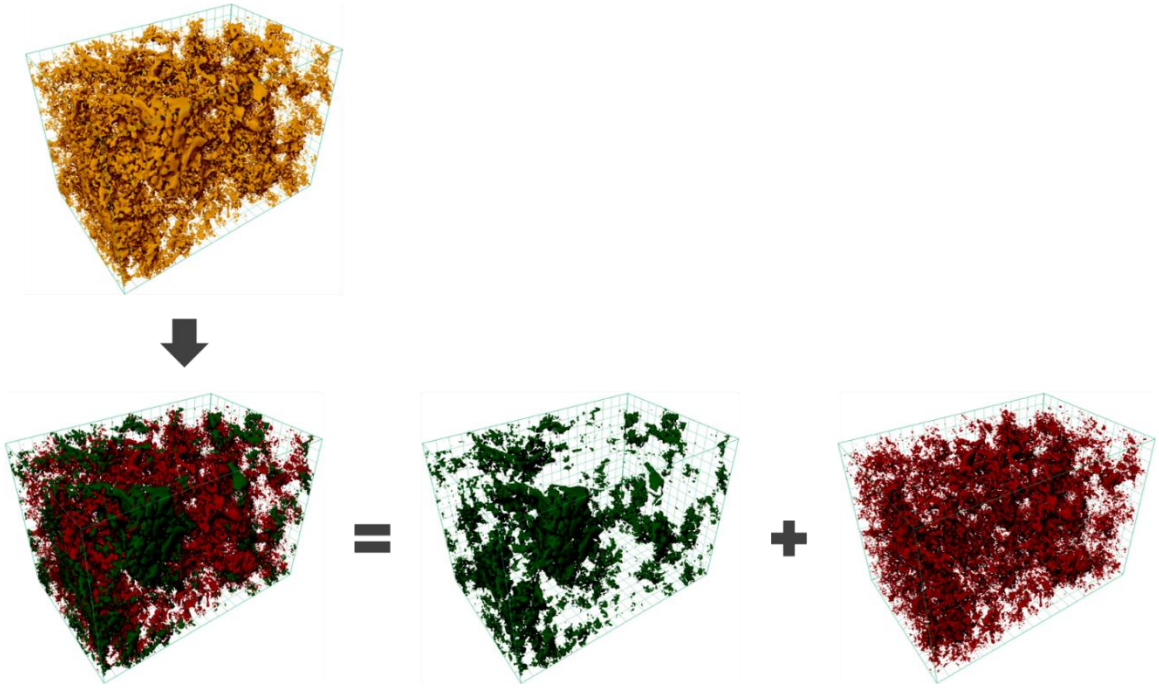

Fig. 14. Total porosity (green-colored 3D model) of the ROI-2 separated into connected (effective) porosity (green-colored 3D model) and non-connected (isolated) porosity (red-colored 3D model).

Fig. 15 depicts a relationship between pore diameter, pore volume, and pore surface of the total porosity 3D model of the ROI-1 and ROI-2. As shown in the graphs, pores within both 3D models show similar distribution.

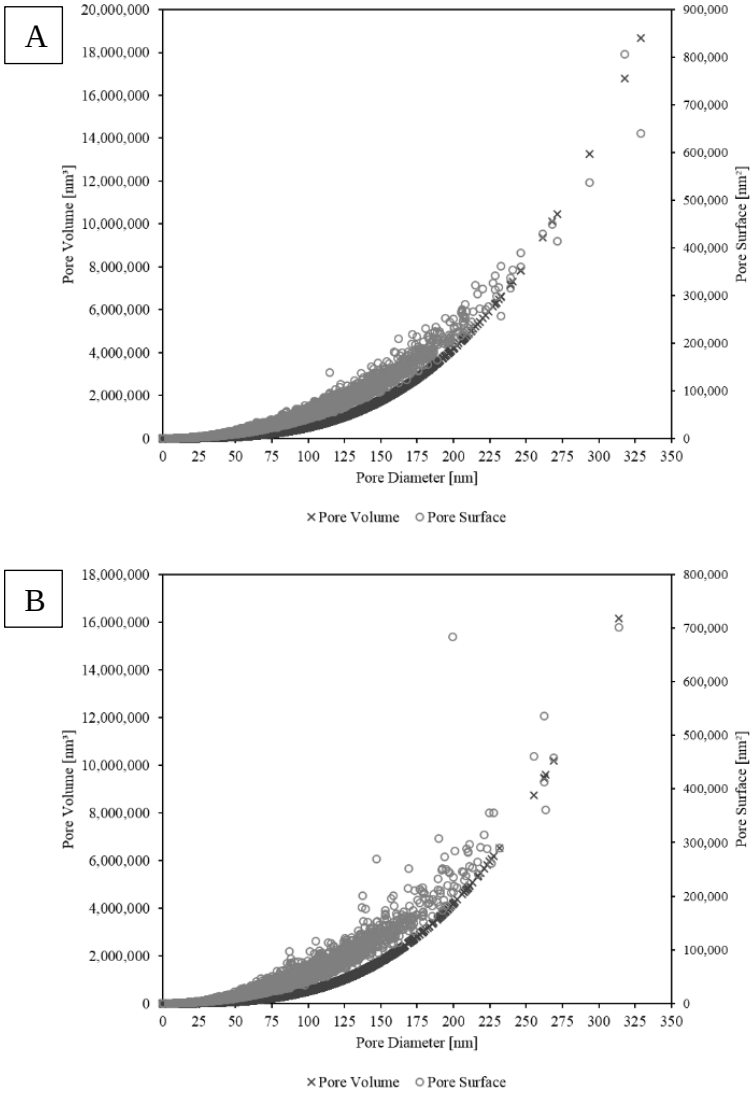

Fig. 15. Graph of pore volume, pore diameter, and pore surface relationship of the total porosity within (A) the ROI-1, and (B) the ROI-2 3D model. Pore volume/surface was calculated based on the total number of voxels of each pore, whereas pore diameter was calculated based on the maximum diameter of an inscribed circle drawn inside of each pore.

Fig. 16 and Fig. 17 depict two charts with pore size (diameter) distribution comparing total and connected porosity within both 3D models of the ROI-1 and ROI-2. As shown in these two figures, both 3D models had similar pore size distribution – they both contained pores with diameter that varied from approximately 5 nm to 330 nm, where about 95% of these pores were

smaller than approximately 80 nm in diameter (as shown by cumulative pore count (of the total porosity) curve in both graphs). Also, when PSDs of the total and connected porosity 3D models are compared, it can be observed that the vast majority of these pores were poorly connected. Only a small fraction of the total-porosity pores (contained in the yellow bins of both the PSD histograms) contributed to the connected porosity (green bins). Although connected porosity of the ROI-1 and ROI-2 accounted for 60.9% and 45.9% of the total pore volume, respectively, it was only due to fewer larger pores contributing to the connected porosity, as shown at the end of each of the histograms where yellow and green bins overlapped with each other. It should be noted that the apparent blip in the pore count at diameters about 180 nm in Fig. 16 and 17 is an artefact due to a switch from using 3-nm bins to 30-nm bins to accommodate the low pore count at these higher diameters. If 3-nm bins were used throughout, the pore count would continue its almost smooth decline.

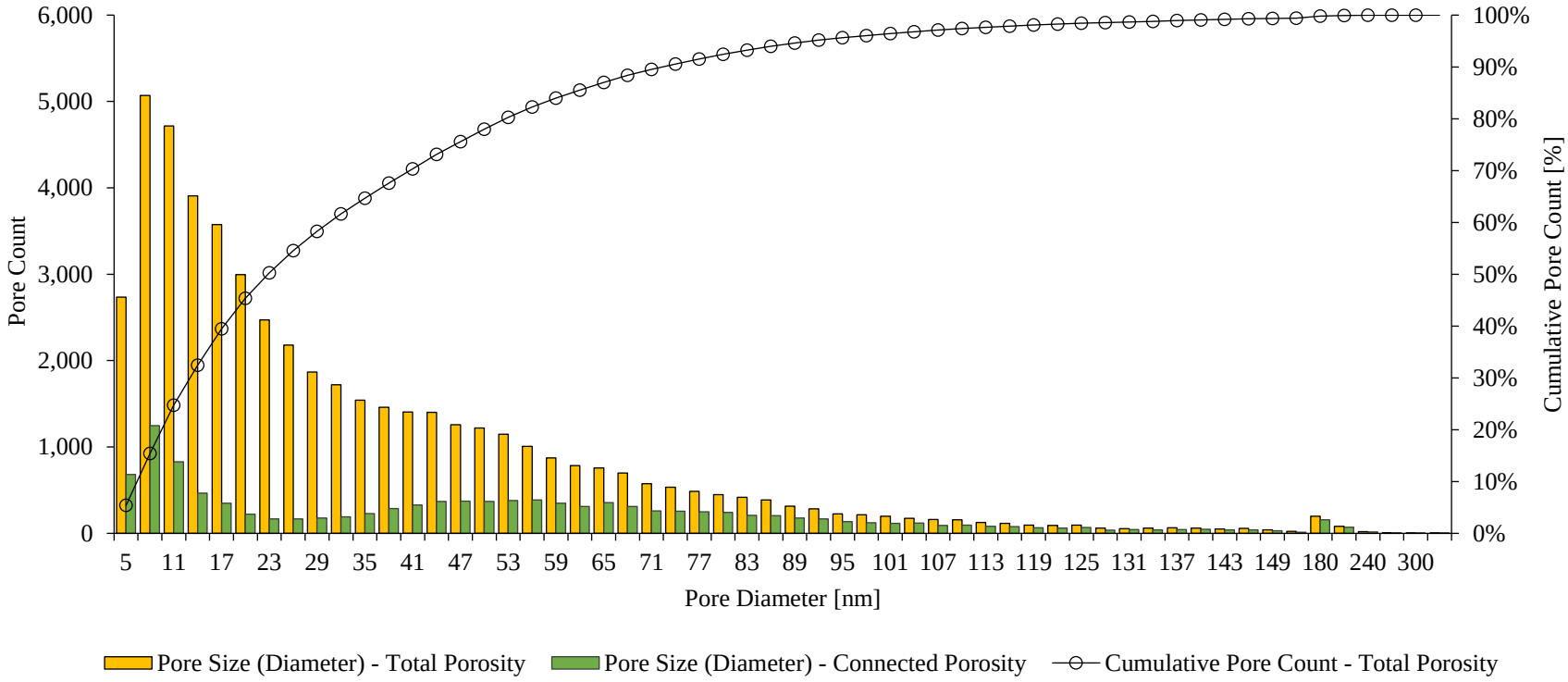

Fig. 16. Pore size (diameter) distribution (pore count as a function of their diameter) of total and connected organic-mater-hosted porosity within the first region of interest (ROI-1) 3D model.

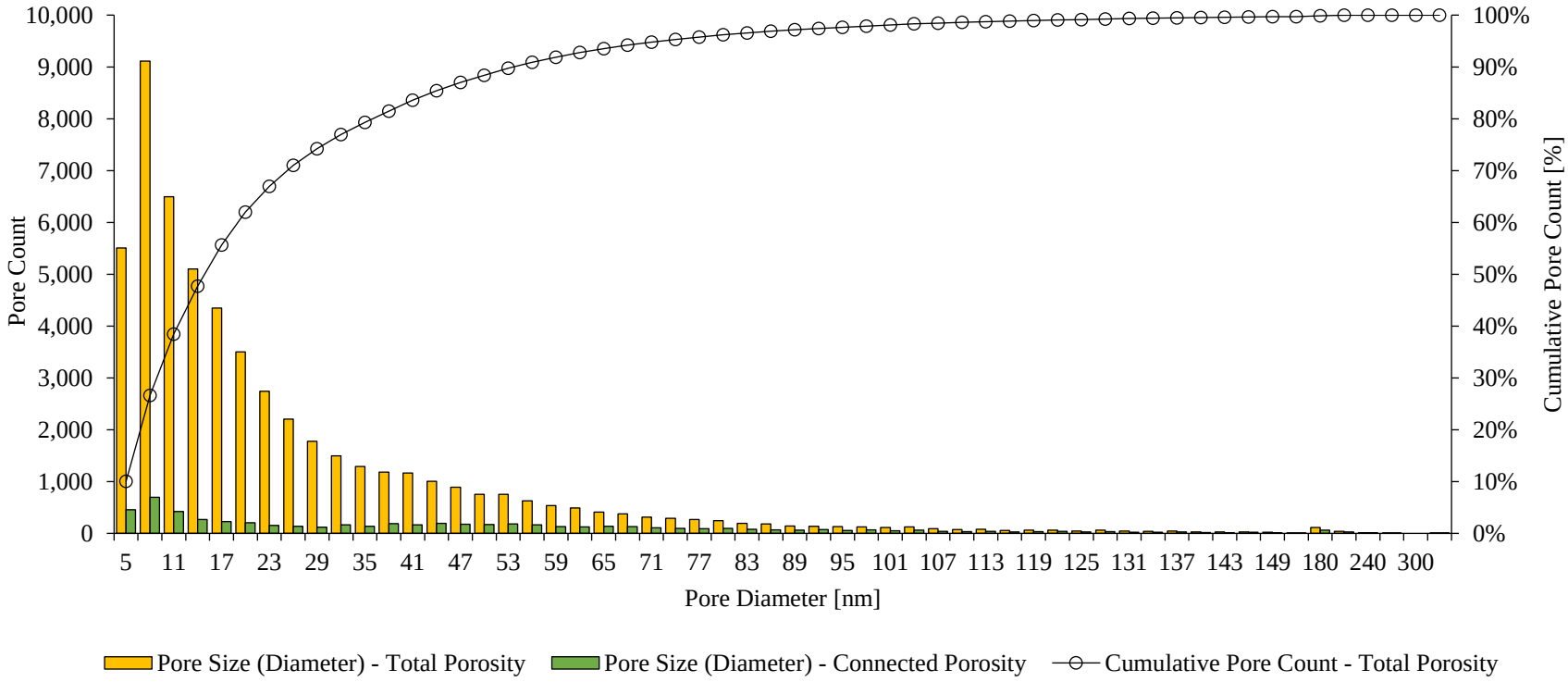

Fig. 17. Pore size (diameter) distribution (pore count as a function of their diameter) of total and connected organic-hosted porosity within the second region of interest (ROI-2) 3D model.

The vast majority of the organic-hosted pores were ineffective in terms their connectivity. Low interconnectivity of these pores is due to their almost spherical geometry. This can be observed by plotting a log-log graph of pore volume versus its diameter, which shows linear trend, as shown in Fig. 18. A good fit to the data is a straight line of slope 3. This is consistent with the pores being spherical or at least closed with a diameter interpreted as an effective diameter (i.e., $V = \pi d^{3/6}$).

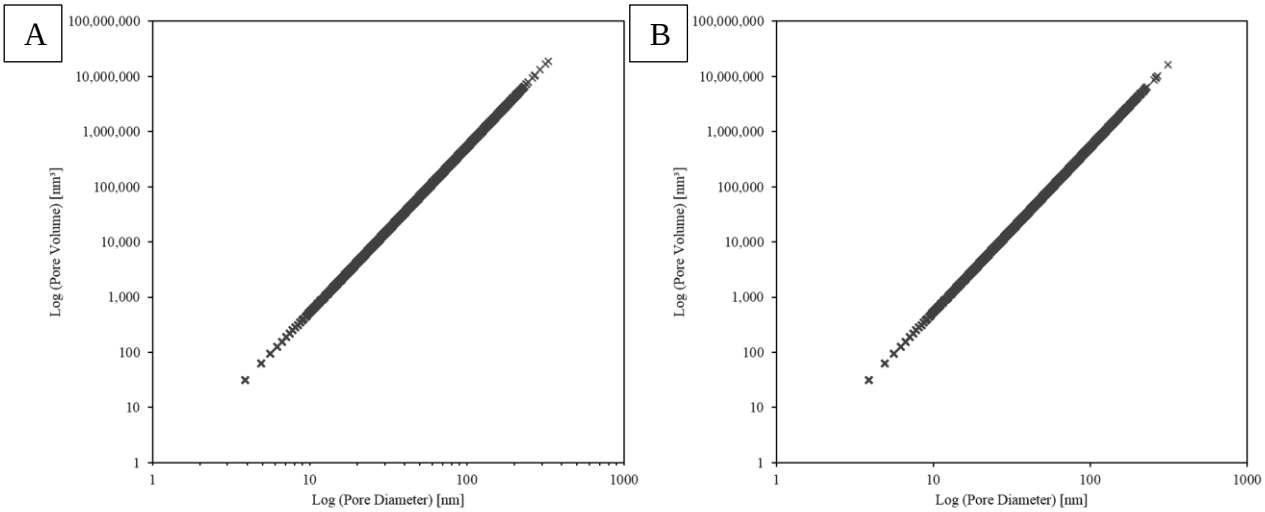

Fig. 18. Logarithmic graph of pore volume vs. pore diameter of the total porosity within (A) the ROI-1, and (B) ROI-2 3D model.

3.2.3. Porosity and Flow Rate Distribution Analysis using Bundle-of-Capillaries Model

Recently, a method of estimating the impact of the pore size distribution on the porosity and flow rate of core (shale) rock samples has been developed (Walton, 2019). The basis of the model is to represent the connected pore structure by a simple bundle of capillaries whose diameter distribution reflects the measured pore size distribution. Note that although majority of the organic-hosted pores have spherical shape, a simplification of treating them as a bundle-of-capillaries was assumed for the purpose of applying this model. The porosity of the connected pore system then depends on the square of the diameter of the pores, as shown in equation 1;

$$\frac{\emptyset_n}{\emptyset} = \frac{f_n d_n^2}{\sum_1^{N_b} f_n d_n^2}, \qquad (1)$$

while the distribution of flow rate through the pores structure depends on the fourth power of the diameters of the tubes, as shown in equation 2;

$$\frac{q_n}{q} = \frac{f_n d_n^4}{\sum_1^{N_b} f_n d_n^4}, \qquad (2)$$

where

f_n – frequency distribution (number of pores per bin),

d_n – average pore diameter (bin size),

N_b – number of bins.

Applying this technique to the pore size distribution of the connected porosity 3D models shown in Fig. 16 and Fig. 17, the porosity and flow rate distributions can be calculated and are shown in Fig. 19 (for ROI-1) and Fig. 20 (for ROI-2). Again, it is convenient to break down the distribution into two groups – one for pores less than 150 nm in diameter and a second one for the relatively few larger pores. The two plots together indicate a shift of the porosity to the larger pores and, perhaps more significantly, a major shift of the flow rate to the few larger pores.

These findings suggest that traditional laboratory methods of estimating the effective porosity and permeability of core (shale) rock samples may be compromised by the inability to capture the details of the connected pore structure, particularly in identifying and measuring the relatively few larger pores. Therefore, caution should be exercised when considering bulk-measured porosities of representative of storage in shales and highlight the role larger pores play in contributing to flow capacity.

It should be re-emphasized the conclusion drawn earlier, that the porosity of a sample associated with the connected pore structure represents only a small part of the total porosity. It has been assumed in this analysis that the non-connected pores do not contribute to the flow capacity of the sample.

Although it is difficult to arrive at a consensus, it is likely that most of the pores within the organic matter are very small (with diameter typically smaller than about 100 nm) and are not connected to one another. Even on the basis of this superficial discussion, it seems likely that most of the hydrocarbon production is via larger connected inter-particle pores or micro-fractures, and not the organic-hosted pores.

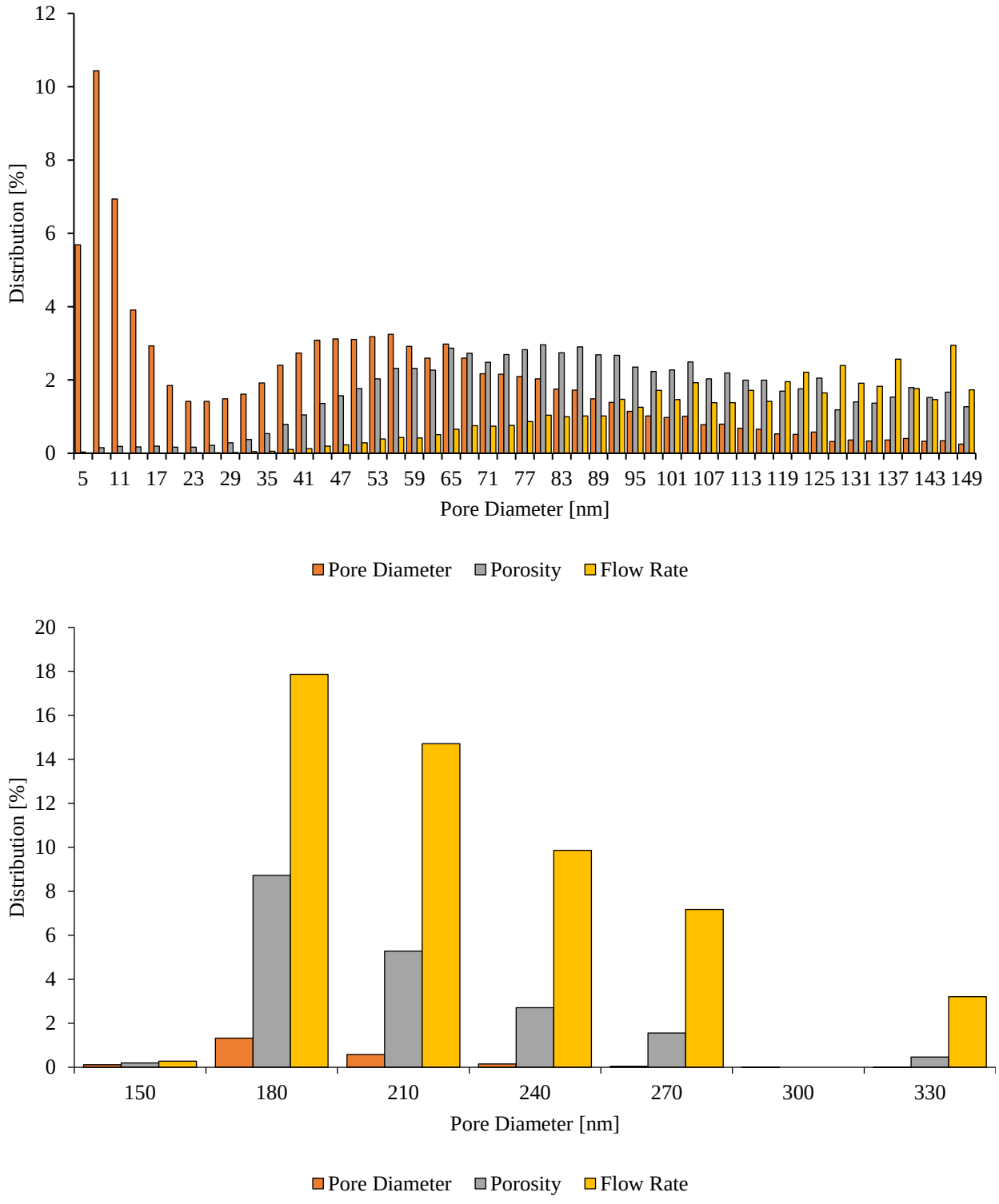

Fig. 19. Porosity and flow rate distribution within the connected porosity 3D model of the ROI-1.

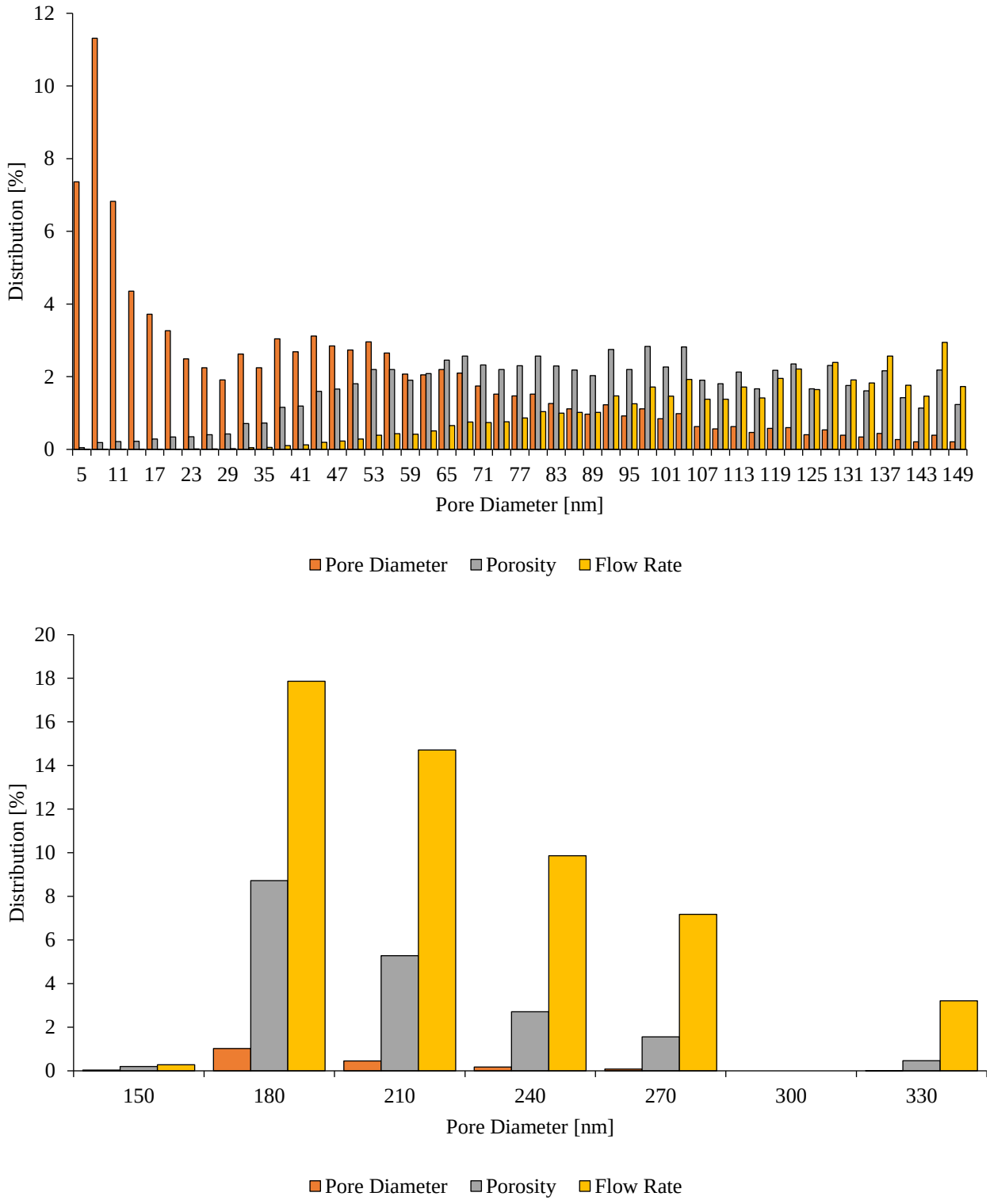

Fig. 20. Porosity and flow rate distribution within the connected porosity 3D model of the ROI-2.

4. Conclusions

In this study, the impact of typical pore size distributions on estimates of the effective porosity of shales was investigated using digital rock 3D models reconstructed from machine-learning segmented FIB-SEM nano-tomography image datasets (collected at ultra-high-resolution – voxel size: 2.5 nm x 2.5 nm x 5 nm) of two organic-rich regions of a Vaca Muerta Shale rock sample. It was shown that although most of the pores typically found in shales have pore diameter smaller than about 100 nm, most of the hydrocarbon production is carried by a relatively small number of larger connected pores with pore diameter greater than about 150 nm. Therefore, there is significant evidence to support that a large portion of the organic-hosted pores (with diameter typically smaller than about 100 nm) do not provide permeable flow pathways for the oil and/or gas migration, and hence have very little contribution to the hydrocarbon production.

References

Andrew, Matthew. "*A quantified study of segmentation techniques on synthetic geological XRM and FIB-SEM images.*" Computational Geosciences 22 (2018): 1503-1512.

Anovitz, Lawrence M., and David R. Cole. "*Characterization and analysis of porosity and pore structures.*" Reviews in Mineralogy and Geochemistry 80, no. 1 (2015): 61-164.

Badessich, M. Fernandez, Damian E. Hryb, Mariano Suarez, Laurent Mosse, Nuncio Palermo, Stephane Pichon, Laurence Reynolds. "*Vaca Muerta Shale: Taming a giant.*" Oilfield Review 28, no. 1 (2016): 26-39.

Berg, Steffen, Nishank Saxena, Majeed Shaik, Chaitanya Pradhan. "*Generation of ground truth images to validate micro-CT image-processing pipelines.*" The Leading Edge 37, no. 6 (2018): 412-420.

Breiman, Leo. "*Random Forests.*" Machine Learning 45, no. 1 (2001): 5-32.

Cavanaugh, Timothy, and Joel Walls. "*Multiresolution imaging of shales using electron and helium ion microscopy.*" Memoir 112: Imaging Unconventional Reservoir Pore Systems, AAPG Special Volumes (2016): 65-76.

Chauhan, Swarup, Wolfram Rühaak, Faisal Khan, Frieder Enzmann, Philipp Mielke, Michael Kersten, Ingo Sass. "*Processing of rock core microtomography images: Using seven different machine learning algorithms.*" Computers and geosciences 86 (2016): 120-128.

Chalmers, Gareth R., R. Marc Bustin, Ian M. Power. "*Characterization of gas shale pore systems by porosimetry, pycnometry, surface area, and field emission scanning electron microscopy/transmission electron microscopy image analyses: Examples from the Barnett, Woodford, Haynesville, Marcellus, and Doig units.*" AAPG Bulletin 96, no. 6 (2012): 1099-1119.

Curtis, Mark E., Brian J. Cardott, Carl H. Sondergeld, Chandra S. Rai. "*Development of organic porosity in the Woodford Shale with increasing thermal maturity.*" International Journal of Coal Geology 103 (2012a): 26-31.

Curtis, Mark E., Carl H. Sondergeld, Raymond J. Ambrose, Chandra S. Rai. "*Microstructural investigation of gas shales in two and three dimensions using nanometer-scale resolution imaging.*" AAPG Bulletin 96, no. 4 (2012b): 665-677.

Curtis, Mark Erman, Raymond Joseph Ambrose, Carl H. Sondergeld, Chandra Shekhar Rai. "*Investigation of the relationship between organic porosity and thermal maturity in the Marcellus Shale.*" North American Unconventional Gas Conference and Exhibition. Society of Petroleum Engineers (2011a).

Curtis, Mark Erman, Raymond Joseph Ambrose, Carl H. Sondergeld, Chandra Shekhar Rai. "*Transmission and scanning electron microscopy investigation of pore connectivity of gas shales on the nanoscale.*" North American Unconventional Gas Conference and Exhibition. Society of Petroleum Engineers (2011b).

Driskill, Brian, Joel Walls, Juliana DeVito, Steven W. Sinclair. "*Applications of SEM imaging to reservoir characterization in the Eagle Ford Shale, South Texas, USA.*" AAPG Memoir 102: Electron Microscopy of Shale Hydrocarbon Reservoirs, AAPG Special Volumes (2013): 115-136.

Goldstein, Joseph I., Dale E. Newbury, Joseph R. Michael, Nicholas WM Ritchie, John Henry J. Scott, David C. Joy. Scanning electron microscopy and X-ray microanalysis. Springer, 2017.

Goral, Jan, Milind Deo, Matthew Andrew. "*Correlative multiscale imaging of Mancos Shale.*" International Petroleum Technology Conference. Society of Petroleum Engineers (2019).

Goral, Jan, Milind Deo, Matthew Andrew. "*Pore network modeling of Marcellus Shale using digital rock analysis with machine learning image segmentation.*" ZEISS Application Note (2018).

Goral, Jan, Ilija Miskovic, Jeff Gelb, Mike Marsh. "*Correlative X-ray and electron microscopy for multi-scale characterization of heterogeneous shale reservoir pore systems.*" Memoir 112: Imaging Unconventional Reservoir Pore Systems, AAPG Special Volumes (2016).

Goral, Jan, Ilija Miskovic, Jeff Gelb, Jack Kasahara. "*Pore network investigation in Marcellus Shale rock matrix.*" SPE Asia Pacific Unconventional Resources Conference and Exhibition. Society of Petroleum Engineers (2015a).

Goral, Jan, Ilija Miskovic, Jeff Gelb, Matthew Andrew. "*Correlative XRM and FIB-SEM for (non)organic pore network modeling in Woodford shale rock matrix.*" International Petroleum Technology Conference. Society of Petroleum Engineers (2015b).

Ji, Liming, Tongwei Zhang, Kitty L. Milliken, Junli Qu, and Xiaolong Zhang. "*Experimental investigation of main controls to methane adsorption in clay-rich rocks.*" Applied Geochemistry 27, no. 12 (2012): 2533-2545.

Jones, Anthony C., Christoph H. Arns, Adrian P. Sheppard, Dietmar W. Hutmacher, Bruce K. Milthorpe, and Mark A. Knackstedt. "*Assessment of bone ingrowth into porous biomaterials using MICRO-CT*." Biomaterials 28, no. 15 (2007): 2491-2504.

Klein, Cornelis, Barbara Dutrow, James D. Dana. "*The 23rd edition of the manual of mineral science*". (2007).

Koebernick, N., Daly, K.R., Keyes, S.D., George, T.S., Brown, L.K., Raffan, A., Cooper, L.J., Naveed, M., Bengough, A.G., Sinclair, I., Hallett, P.D., Roose, T. "*High-resolution synchrotron imaging shows that root hairs influence rhizosphere soil structure formation.*" *New Phytologist* 216, no. 1 (2017): 124-135.

Loucks, Robert G., Robert M. Reed. "*Scanning-electron-microscope petrographic evidence for distinguishing organic-matter pores associated with depositional organic matter versus migrated organic matter in mudrock.*" GCAGS Journal (2014).

Loucks, Robert G., Robert M. Reed, Stephen C. Ruppel, Ursula Hammes. "*Spectrum of pore types and networks in mudrocks and a descriptive classification for matrix-related mudrock pores.*" AAPG bulletin 96, no. 6 (2012): 1071-1098.

Loucks, Robert G., Robert M. Reed, Stephen C. Ruppel, Daniel M. Jarvie. "*Morphology, genesis, and distribution of nanometer-scale pores in siliceous mudstones of the Mississippian Barnett Shale.*" Journal of Sedimentary Research 79, no. 12 (2009): 848-861.

Mehmani, Ayaz, Masa Prodanovic, Farzam Javadpour. "*Multiscale, multiphysics network modeling of shale matrix gas flows.*" Transport in Porous Media 99, no. 2 (2013): 377-390.

Milliken, Kitty L., and Mark E. Curtis. "*Imaging pores in sedimentary rocks: foundation of porosity prediction.*" Marine and Petroleum Geology 73 (2016): 590-608.

Milliken, Kitty L., Mark Rudnicki, David N. Awwiller, Tongwei Zhang. "*Organic matter–hosted pore system, Marcellus formation (Devonian), Pennsylvania.*" AAPG bulletin 97, no. 2 (2013): 177-200.

Nelson, Philip H. "*Pore-throat sizes in sandstones, tight sandstones, and shales.*" AAPG bulletin 93, no. 3 (2009): 329-340.

Otsu, Nobuyuki. "*A threshold selection method from gray-level histograms.*" IEEE Transactions on Systems, Man, and Cybernetics 9, no. 1 (1979): 62-66.

Pommer, Maxwell, and Kitty Milliken. "*Pore types and pore-size distributions across thermal maturity, Eagle Ford Formation, southern Texas*" AAPG Bulletin 99, no. 9 (2015): 1713-1744.

Schweizer, Steffen A., Carmen Hoeschen, Steffen Schlüter, Ingrid Kögel-Knabner, Carsten W. Mueller. "*Rapid soil formation after glacial retreat shaped by spatial patterns of organic matter accrual in microaggregates.*" Global Change Biology 24, no. 4 (2018): 1637-1650.

Shabro, Vahid, Carlos Torres-Verdin, and Farzam Javadpour. "*Numerical simulation of shale-gas production: from pore-scale modeling of slip-flow, Knudsen diffusion, and Langmuir desorption to reservoir modeling of compressible fluid.*" North American Unconventional Gas Conference and Exhibition. Society of Petroleum Engineers (2011).

Slatt, Roger M., and Neal R. O'Brien. "*Pore types in the Barnett and Woodford gas shales: Contribution to understanding gas storage and migration pathways in fine-grained rocks.*" AAPG bulletin 95, no. 12 (2011): 2017-2030.

Song, Liaosha, Keithan Martin, Timothy R. Carr, Payam Kavousi Ghahfarokhi. "*Porosity and storage capacity of Middle Devonian shale: A function of thermal maturity, total organic carbon, and clay content.*" Fuel 241 (2019): 1036-1044.

Walton, Ian C. *"Impact of Pore Size Distribution on Shale Production, Permeability, and Porosity."* In preparation (2019).

Xia, Yidong, Jan Goral, Hai Huang, Ilija Miskovic, Paul Meakin, Milind Deo. "*Many-body dissipative particle dynamics modeling of fluid flow in fine-grained nanoporous shales.*" Physics of Fluids (2017).

Zhang, Tongwei, Geoffrey S. Ellis, Stephen C. Ruppel, Kitty Milliken, Rongsheng Yang. "*Effect of organic-matter type and thermal maturity on methane adsorption in shale-gas systems.*" Organic Geochemistry 47 (2012): 120-131.

Zhang, Pengwei, Liming Hu, Jay N. Meegoda, Shengyan Gao. "*Micro/nano-pore network analysis of gas flow in shale matrix.*" Scientific Reports 5 (2015): 13501.